Optimization of layer thickness, doping concentration, defect density, and operating temperature for enhanced performance of $RbGeBr_3$ - based solar cells

ANCHAL SRIVASTAVA[1], SHOBHIT SHUKLA[2,*], R. K. SHUKLA[1], K. C. DUBEY[3], NIDHI SINGH[1]
[1]*Department of Physics, University of Lucknow, Lucknow-226007, India*
[2]*Department of Information Technology, Dr. S.M.N.R. University, Lucknow-226017, India*
[3]*Department of Physics, Shia P.G. College, Lucknow-226020, India*

This study explores a novel lead-free perovskite solar cell using $RbGeBr_3$, showing potential for high power conversion efficiency and stability. To enhance its efficiency for practical applications, a detailed analysis was conducted using SCAPS-1D to optimize the device architecture. The study focuses on utilizing Cu_2O as the hole transport layer and ZnO as the electron transport layer to improve overall performance. Key parameters, including layer thickness, doping concentration, defect density, series and shunt resistance and operating temperature, were meticulously optimized. The parametric study resulted in remarkable outcomes, achieving a short-circuit current density of 26.04 $mA \cdot cm^{-2}$, an open-circuit voltage of 1.09 V, a fill factor of 87.26%, and a power conversion efficiency of 24.86%.

(Received April 16, 2025; accepted December 2, 2025)

Keywords: SCAPS simulation, Solar cell, Photovoltaic, Lead-free perovskite, $RbGeBr_3$, Power conversion efficiency

1. Introduction

The emphasis on renewable energy has surged globally as the need for clean and sustainable energy sources intensifies. Among various renewable technologies, solar cells have garnered significant attention due to the abundance, renewability, and eco-friendliness of sunlight, contrasting with finite fossil fuels [1-2]. Over the past decade, metal halide perovskites have gained remarkable importance in the photovoltaic field, achieving power conversion efficiencies (PCEs) exceeding 25% [3-5]. However, the primary challenge hindering widespread adoption lies in the lead content of current metal halide perovskite formulations, conflicting with strict anti-lead regulations in electronics [6].

To address this, research has shifted towards lead-free alternatives by substituting lead with less toxic elements like tin, bismuth, antimony, copper, or germanium in $APbX_3$ perovskite structures [7]. Notably, tin-based perovskites [8-10] have shown promising PCEs of up to 13% along with advantages such as lower optical bandgaps [11–13] and enhanced charge mobility [14] compared to lead-based counterparts. Despite their potential, stability issues persist, particularly concerning oxidation under ambient conditions due to potential trap formation [15-16].

Although lead-free perovskites have exhibited commendable efficiencies [17–20], further improvements in stability and effectiveness are required [21–24], as their PCEs remain below the Shockley - Queisser efficiency limit of 33.7% for a single junction [25]. Notably, this limit has been exceeded in perovskite solar cells (PSCs) through nanoscale metallization [25–28]. To combat oxidation, several strategies are being explored, including electronic structure modifications, encapsulation, hydrogen bonding integration, and hydrophobic layer applications [29–33]. To bridge the efficiency gap with lead-based perovskites, ongoing research focuses on enhancing PCEs [34-35].

The parameters of solar cell can be obtained by solving the fundamental equations that dictate the charge transport in semiconductors, listed as follows. Poisson equation:

$$\frac{dE}{dx} = -\frac{d^2\Psi}{dx^2} = \frac{q}{\varepsilon}[p(x) - n(x) + N_D^+(x) - N_A^-(x) + p_t(x) - n_t(x)] \quad (1)$$

In this perspective, 'E' represents the electric field, 'Ψ' denotes the electrostatic potential, 'q' stands for the electron charge, 'ε' symbolizes the dielectric constant of the semiconductor material, 'p' and 'n' represent the concentrations of holes and electrons respectively. Additionally, N_A^- and N_D^+ reflect the densities of ionized acceptors and donors, while 'n_t' and 'p_t' signify trapped electrons and holes. Finally, 'x' corresponds to the positional coordinate in the formulation.

The continuity Eq.(2) for holes and Eq.(3) for electrons are

$$\frac{dp_n}{dt} = G_p - \frac{p_n - p_{no}}{\tau_p} + p_n\mu_p\frac{dE}{dx} + \mu_p E\frac{dp_n}{dx} + D_p\frac{d^2p_n}{dx^2} \quad (2)$$

$$\frac{dn_p}{dt} = G_n - \frac{n_p - n_{po}}{\tau_n} + n_p\mu_n\frac{dE}{dx} + \mu_n E\frac{dn_p}{dx} + D_n\frac{d^2n_p}{dx^2} \quad (3)$$

where G_n and G_p are the electron and hole generation rates, D_n and D_p are the hole and electron diffusion coefficients.

The carrier transport occurs by the diffusion and the drift is expressed as follows:

$$J_n(x) = qn\mu_n E + qD_n\frac{dn}{dx} = n\mu_n\frac{dE_{Fn}}{dx} \quad (4)$$

$$J_p(x) = qp\mu_p E + qD_p\frac{dp}{dx} = p\mu_p\frac{dE_{Fp}}{dx} \quad (5)$$

where μ_p and μ_n represent the mobility's of holes and electrons, respectively, and E_{Fn} and E_{Fp} denote the quasi-Fermi levels for electrons and holes.

In this contribution, we aim to enhance the efficiency of $RbGeBr_3$-based solar cells using SCAPS software, developed by Gent University [36]. The simulation focuses on employing metal oxide transport layers, particularly ZnO, chosen for their suitable electronic properties, high transparency, and uniform substrate coverage. These characteristics make them excellent candidates for electron transport layers in the cost-effective, large-scale production of lead-free perovskite solar cells [37-38].

There are currently no published experimental research papers reporting the key photovoltaic parameters for $RbGeBr_3$ solar cells. Most available studies on $RbGeBr_3$ devices are based on simulations and theoretical modeling, rather than actual device fabrication and measurement. The highest reported data for an $RbGeBr_3$-based device comes from numerical modeling where, for example, one study predicts a power conversion efficiency of 11.89% for an FTO/TiO_2/$RbGeBr_3$/P3HT/Au configuration, but no experimental validation is provided. This lack of experimental data is corroborated in the literature, where authors consistently note that $RbGeBr_3$ perovskite has not yet been synthesized or tested in working solar cell devices, and thus performance metrics remain theoretical. Closely related compositions, such as other inorganic germanium-based perovskites, also largely lack experimental device reports, limiting current understanding to simulation-based estimations.

SCAPS is fundamentally an electrical solver designed for one-dimensional solar cell simulation. It does not inherently model optical absorption and reflection losses but allows users to incorporate these effects explicitly. The photon absorption coefficients must be input manually, either using tabulated data or modeled values for wavelength-dependent absorption. SCAPS calculates generation profiles from these user-supplied absorption coefficients and illumination spectra, such as AM1.5G. Reflection effects can be included via user-defined reflection or transmission data files or approximated externally prior to simulation. This capability ensures that despite SCAPS electrical focus, optical phenomena critical to device performance can be realistically represented when properly implemented in the input parameters.

To achieve maximum efficiency, an optimization process is undertaken. Initially, the layer thickness, doping concentrations, and defect density of the perovskite absorber materials are evaluated and optimized. Subsequently, the same parameters - layer thickness, doping concentrations, and defect density - are optimized for the hole layer and the electron transporting layer. Finally, the results of the optimized structure are presented, demonstrating an efficiency improvement of approximately 24.86%.

2. Materials and methods

The design and performance analysis of the solar cell were conducted using the SCAPS-1D software program, developed by researchers at the University of Gent in Belgium. This numerical simulation tool solves Poisson's and the continuity equations for free holes and electrons in the valence and conduction bands. It enables the computation and observation of various electrical properties and parameters, including the current density–voltage characteristics curve, energy band structure of the heterojunction, quantum efficiency, open circuit voltage, short circuit current density, PCE and fill factor, among others. All simulations were performed at 300K under standard illumination of 1000 W/m² and an air mass of AM 1.5 G.

Fig. 1 illustrates the proposed PSC structure, comprising ITO as the front contact, ZnO as the ETL, $RbGeBr_3$ as the absorber layer, Cu_2O as the HTL, and gold (Au) as the back contact. The solar cell features a conventional (n-i-p) structure, where light enters the cell from the ETL side, with ITO as the front contact and Au as the back contact.

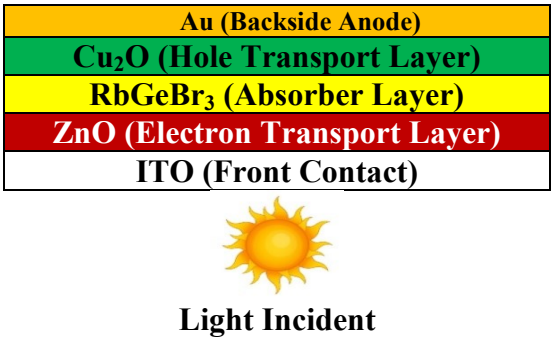

Fig. 1. Schematic structure of ITO/ZnO/$RbGeBr_3$/Cu_2O/Au-based solar cell (colour online)

Table 1 presents the material parameters obtained from theories, experiments, and literature, which were used to establish the initial setup for the simulation process. The parameters include thickness, doping concentrations, and defect density of the ETL, absorber layer, and HTL, as well as the rear metal work function.

These properties were adjusted to optimize performance and evaluate their impact on the device's overall efficiency. Interface defect parameter is shown in Table 2.

Table 1. The initial physical parameters of Cu_2O, $RbGeBr_3$, ZnO and ITO used in the ITO/ZnO/ $RbGeBr_3$/Cu_2O/Au PSC

Physical Parameters	**Symbol**	**Unit**	**Cu_2O (HTL)**	**$RbGeBr_3$**	**ZnO (ETL)**	**ITO**
Thickness	t	nm	100	400	200	100
Energy Band Gap	E_g	eV	2.17	1.49	3.2	3.5
Electron Affinity	X	eV	3.2	3.8	3.75	4.0
Dielectric Permittivity (Relative)	ε_r	-	6.6	7.0	9.0	9.0
Effective Density of States at Valence Band	N_V	cm^{-3}	2.5×10^{20}	2.1×10^{18}	2×10^{20}	1.8×10^{19}
Effective Density of States at Conduction Band	N_C	cm^{-3}	2.5×10^{20}	3.7×10^{19}	1×10^{21}	2.2×10^{18}
Hole Thermal Velocity	V_e	cm/s	1×10^{7}	1×10^{7}	1×10^{7}	1×10^{7}
Electron Thermal Velocity	V_h	cm/s	1×10^{7}	1×10^{7}	1×10^{7}	1×10^{7}
Electron Mobility	μ_e	$cm^2/V.s$	80	850	20	20
Hole Mobility	μ_h	$cm^2/V.s$	80	850	10	10
Uniform Shallow Donor Doping	N_D	cm^{-3}	0	2×10^{13}	1×10^{19}	1×10^{21}
Uniform Shallow Acceptor Doping	N_A	cm^{-3}	3×10^{18}	2×10^{13}	0	0
Defect Density	N_t	cm^{-3}	1×10^{15}	1×10^{15}	1×10^{15}	1×10^{15}
References			39	40	41	42

Table 2. Interface defect parameterization

Interface	Defect types	Cross-sectional capture: holes/electrons (cm^2)	Distribution of energy level	Defect energy level reference	The overall density summed across all energy levels (cm^{-2})
$Cu_2O/RbGeBr_3$	Neutral	$1\times10^{-19}/1\times10^{-19}$	Gaussian	0.6 eV above VB maximum	1×10^{15}
$RbGeBr_3$/ZnO	Neutral	$1\times10^{-19}/1\times10^{-19}$	Gaussian	0.6 eV above VB maximum	1×10^{15}

3. Results and discussion

This section presents the study's findings, beginning with an analysis of how various physical parameters of different layers influence solar cell performance. The investigation involved optimizing the thickness, doping concentrations, and defect density of each layer. All parameters were systematically adjusted to evaluate their impact on the device's overall efficiency and performance.

Changes in thickness, defect density, and doping concentration in the ETL, HTL, and absorber layers physically affect solar cell performance metrics such as V_{oc}, J_{sc}, *FF*, and *PCE*. Increasing absorber thickness generally enhances light absorption, promoting greater generation of electron-hole pairs and increasing J_{sc}. However, beyond an optimal thickness (typically around 400–800 nm depending on the material), carrier recombination increases because photo-generated carriers have longer distances to travel, reducing V_{oc} and *FF* due to recombination losses and increased series resistance. Thus, the *PCE* often peaks at an intermediate absorber thickness balancing absorption and charge collection. ETLs must be thin enough (50–200 nm) to allow maximum photon penetration into the absorber while also sufficient to efficiently transport electrons and block holes, minimizing recombination at contacts. Excessive thickness increases series resistance and light scattering, lowering J_{sc} and *FF*. Similarly, HTL thickness optimization balances charge collection and series resistance. Thickness deviations may also induce surface roughness or pinholes, critically impacting V_{oc} and overall device stability. Increased defect density, particularly in the absorber but also in transport layers, introduces recombination centers that reduce carrier lifetimes, decreasing V_{oc}, J_{sc}, and *FF*. Low defect densities ($<10^{16}$ cm^{-3}) improve charge carrier extraction and enhance *PCE*, while higher defect densities significantly deteriorate device efficiency. Appropriate doping concentrations enhance built-in electric fields,

improving charge separation and transport. Overdoping (>10^{21} cm^{-3}, especially in ETLs like ZnO) is unrealistic and often leads to increased scattering and defect formation, ultimately reducing mobility and efficiency. Moderate doping levels optimize V_{oc} and *FF* by balancing conductivity and recombination suppression.

4. Influence of absorber thickness on the solar cell performance

This section investigates how the absorber material $RbGeBr_3$ influences solar cell performance, focusing on thickness, doping concentration, and defect density. The thickness of the absorber layer in PSCs significantly affects the device's performance by determining light absorption and power conversion efficiency. Optimal thickness is essential: if the layer is too thin, insufficient light is absorbed, resulting in low current generation. Conversely, if it is too thick, charge carriers may struggle to travel through the material to the electrodes, reducing device efficiency. To analyse the impact of absorber thickness on solar cell performance, its value was varied from 25 to 600 nm, with the results depicted in Fig. 2. An increase in J_{sc} was observed with greater absorber thickness due to enhanced photon absorption and electron–hole pair generation. However, V_{oc} decreases with increasing thickness, as a thicker layer introduces a higher defect density, serving as recombination centers. Consequently, the lifetime of electron–hole pairs decreases, leading to increased recombination before reaching the electrodes, thereby reducing V_{oc} and *FF*. The *PCE* of the device increases with thickness up to a maximum value of 22.40% at 600 nm. This pattern arises from the counteracting effects of V_{oc} and J_{sc}, which significantly influence *PCE*.

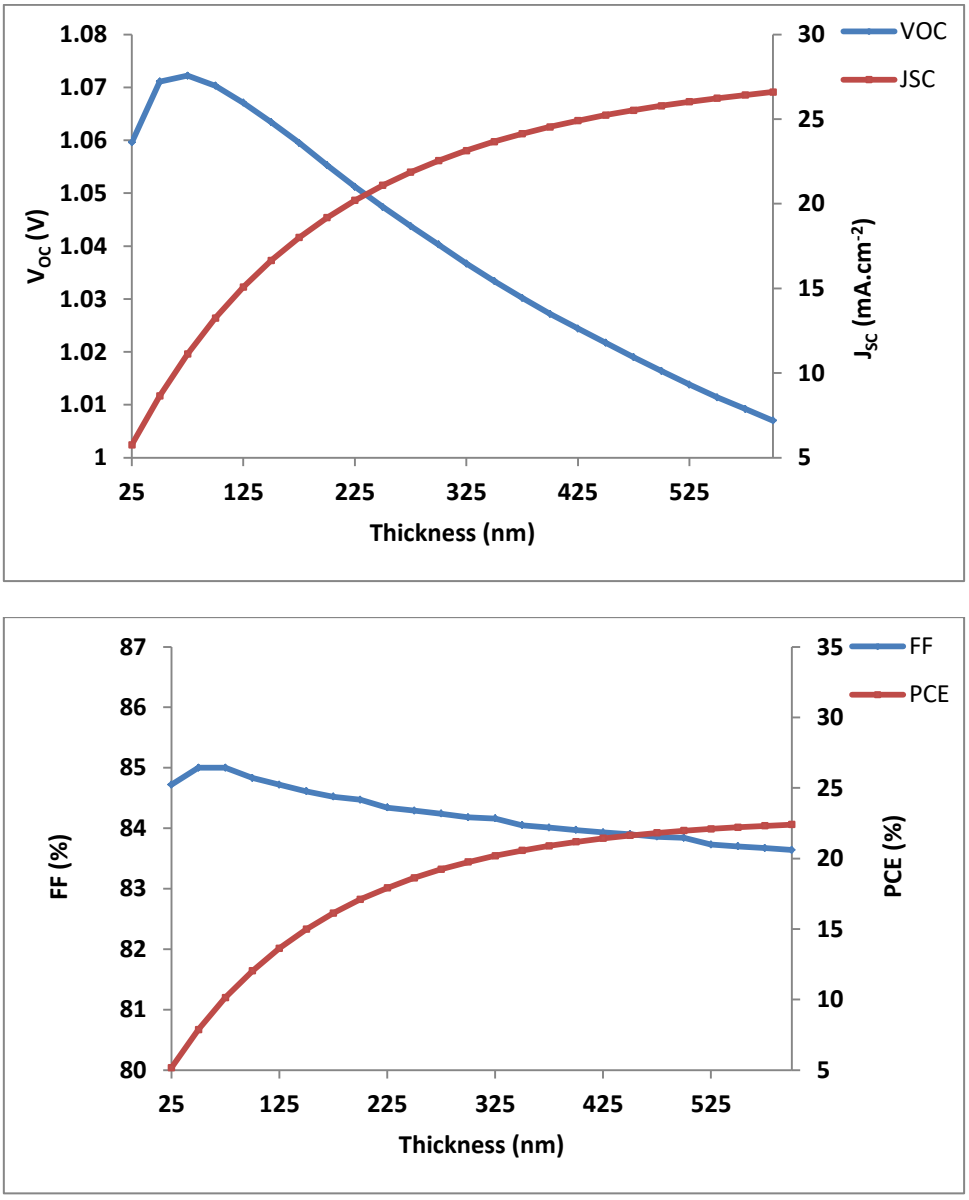

Fig. 2. Variations of V_{oc}, $J_{sc,}$ FF and PCE in terms of the thickness for the Absorber materials ($RbGeBr_3$) (colour online)

5. Impact of absorber doping concentration

Doping is vital for enhancing solar cell performance by influencing carrier density, charge transport, and material stability, thus boosting efficiency. It can be n-type, p-type, or even self-doping, depending on the layer's requirements. However, excessive or improper doping can impair the performance of perovskite materials. To investigate the effect of doping concentration on solar cell performance, the doping level was varied from 1×10^{11} to 1×10^{18} cm^{-3}. Figs. 3 and 4 demonstrate the impact of doping density (N_D) on the performance of the absorber layer, $RbGeBr_3$. Across a broad doping range, performance parameters remain relatively stable, highlighting the material's tolerance to varying doping levels. However, when the doping density exceeds 1×10^{17} cm^{-3}, key parameters such as V_{OC}, J_{SC}, FF and PCE begin to decline. At an optimal doping density of 1×10^{17} cm^{-3}, the solar cell achieves its peak performance, with a PCE of 24.72%, V_{OC} of 1.09 V, J_{SC} of 26.03 mA/cm^2, and FF of 87.42%. Higher doping densities introduce scattering centers and deep traps, reducing carrier mobility and leading to performance degradation. Conversely, variations in p-type doping (N_A) have minimal impact, suggesting a limited role in overall performance as shown in Fig. 4. These findings emphasize the importance of carefully optimizing doping concentrations to maximize efficiency while preserving material stability and charge transport.

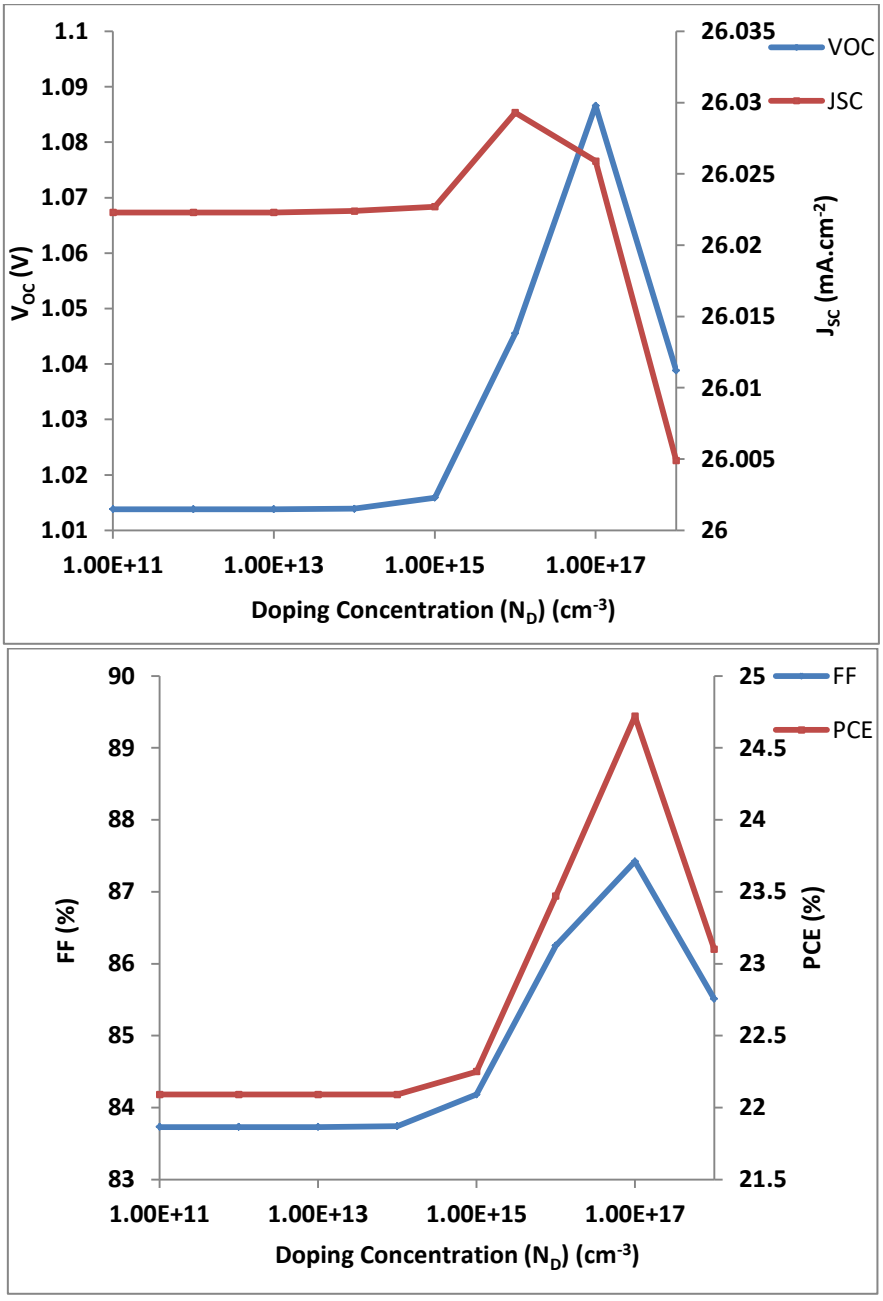

Fig. 3. Variations of V_{oc}, J_{sc}, FF and PCE in terms of the various Doping Concentration (N_D) for the Absorber materials ($RbGeBr_3$) (colour online)

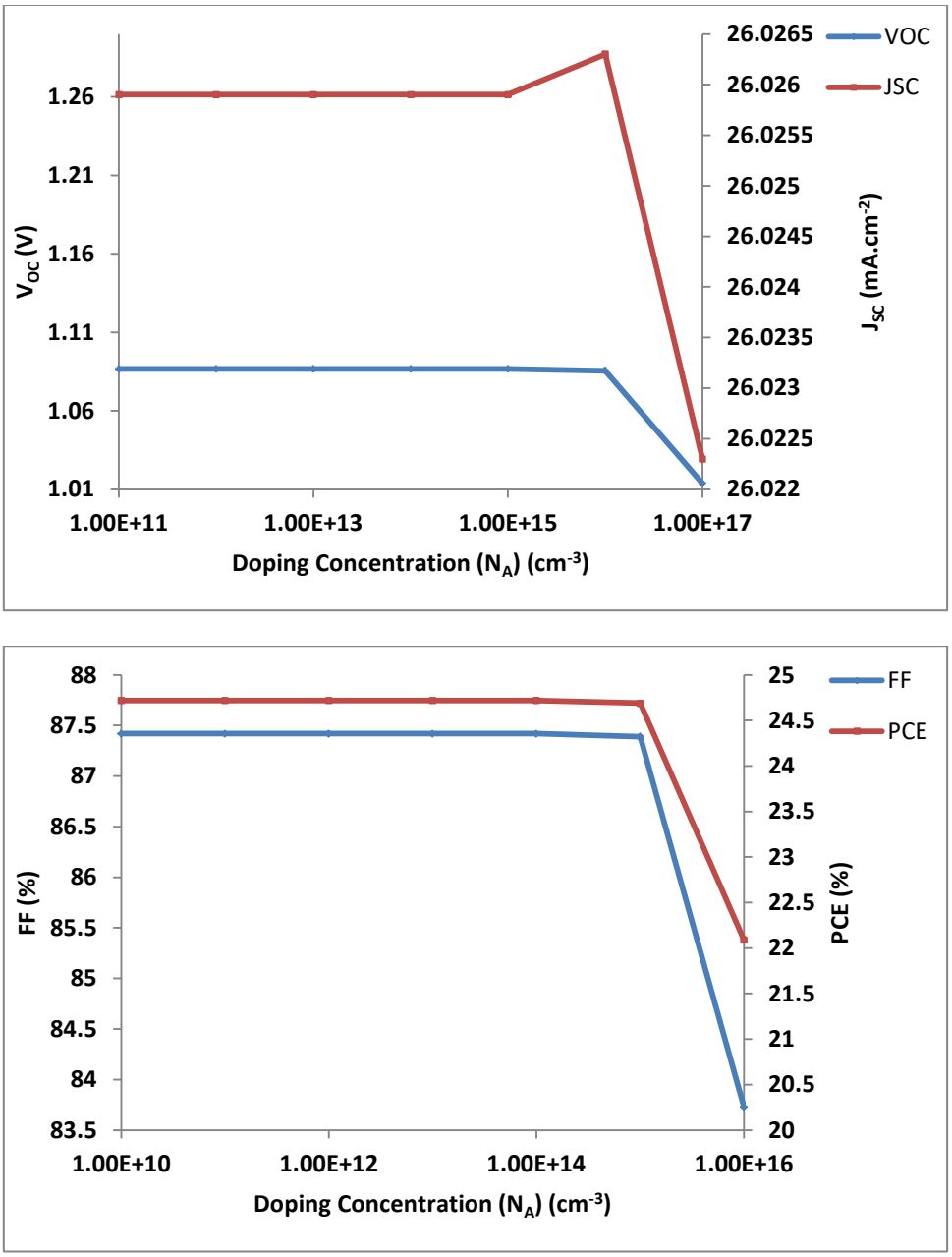

Fig. 4. Variations of V_{oc}, J_{sc}, FF and PCE in terms of the various Doping Concentration (N_A) for the Absorber materials ($RbGeBr_3$) (colour online)

6. Impact of HTL (Cu_2O) thickness

Similar to the preceding sections, variations in absorber thickness significantly influence the performance of PSCs, affecting both efficiency and recombination rates. This study examines HTL thickness within the range of 25–300 nm, integrating the optimized results from earlier sections. The effects on photovoltaic parameters are illustrated in Fig. 5. According to the literature, beyond a certain HTL thickness, the variation in cell parameters becomes minimal [16]. In this study, an optimal HTL thickness of 150 nm is identified, achieving an efficiency of 24.70%.

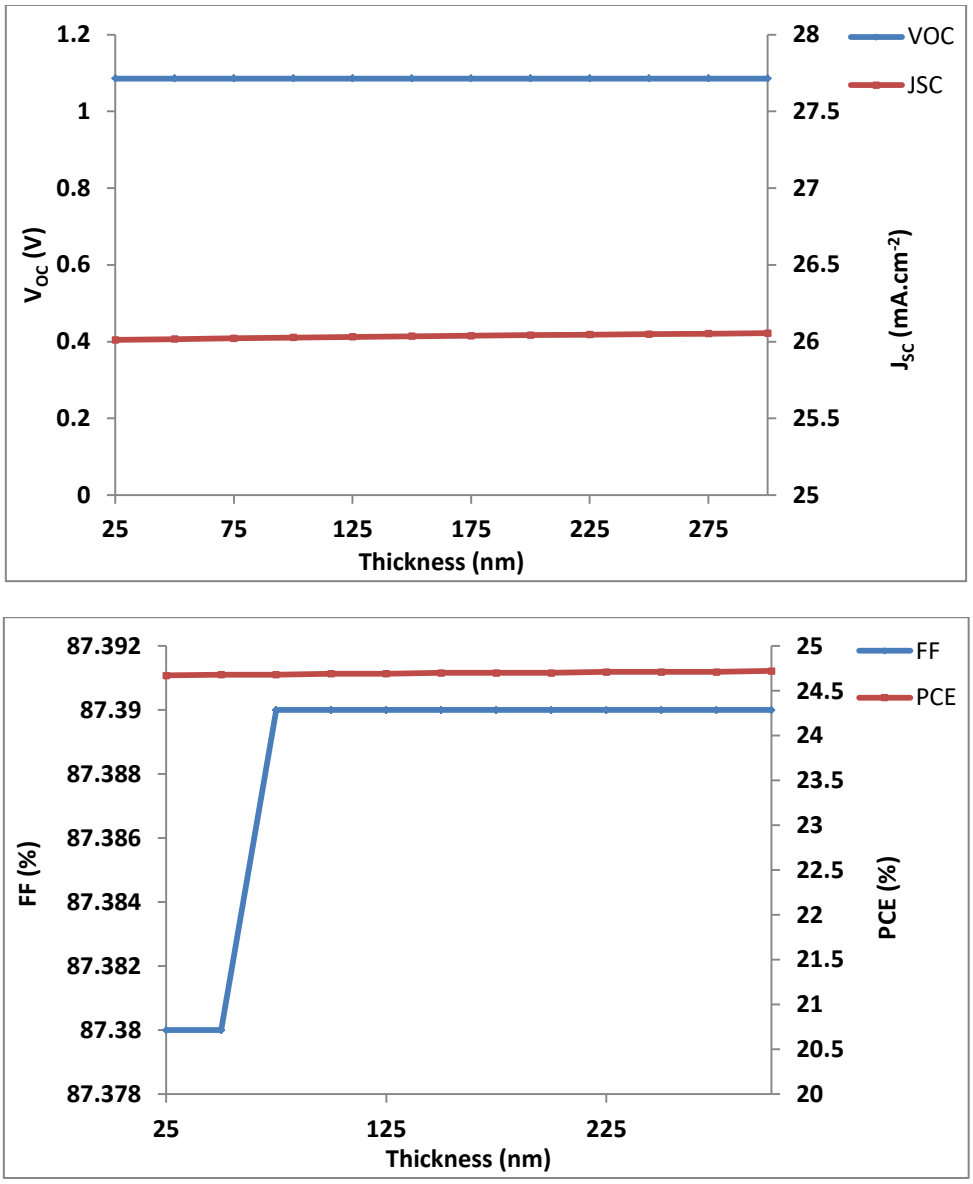

Fig. 5. Variations of V_{oc}, $J_{sc,}$ FF and PCE in terms of the thickness for the HTL materials Cu_2O (colour online)

7. Impact of HTL doping concentration (N_A)

This section explores the effect of HTL doping density variation within the range of 10^{13}–10^{19} cm^{-3} on PSC performance, as illustrated in Fig. 6. The results indicate that efficiency increases with higher doping density due to enhanced hole transporting behaviour at elevated doping levels. However, increased charge density also raises the likelihood of exciton generation, leading to a higher recombination rate. Despite this, the graphs in Fig. 6 show a continuous increase in efficiency across the explored range. The value of $V_{OC,}$ and J_{SC} also rise with increasing HTL doping density. These outcomes indicate that recombination plays a crucial role in determining the optimum doping density. Among the considered values, a doping density of 10^{19} cm^{-3} demonstrates the best performance with a *PCE* of 24.86%, balancing high charge transport and manageable recombination rates.

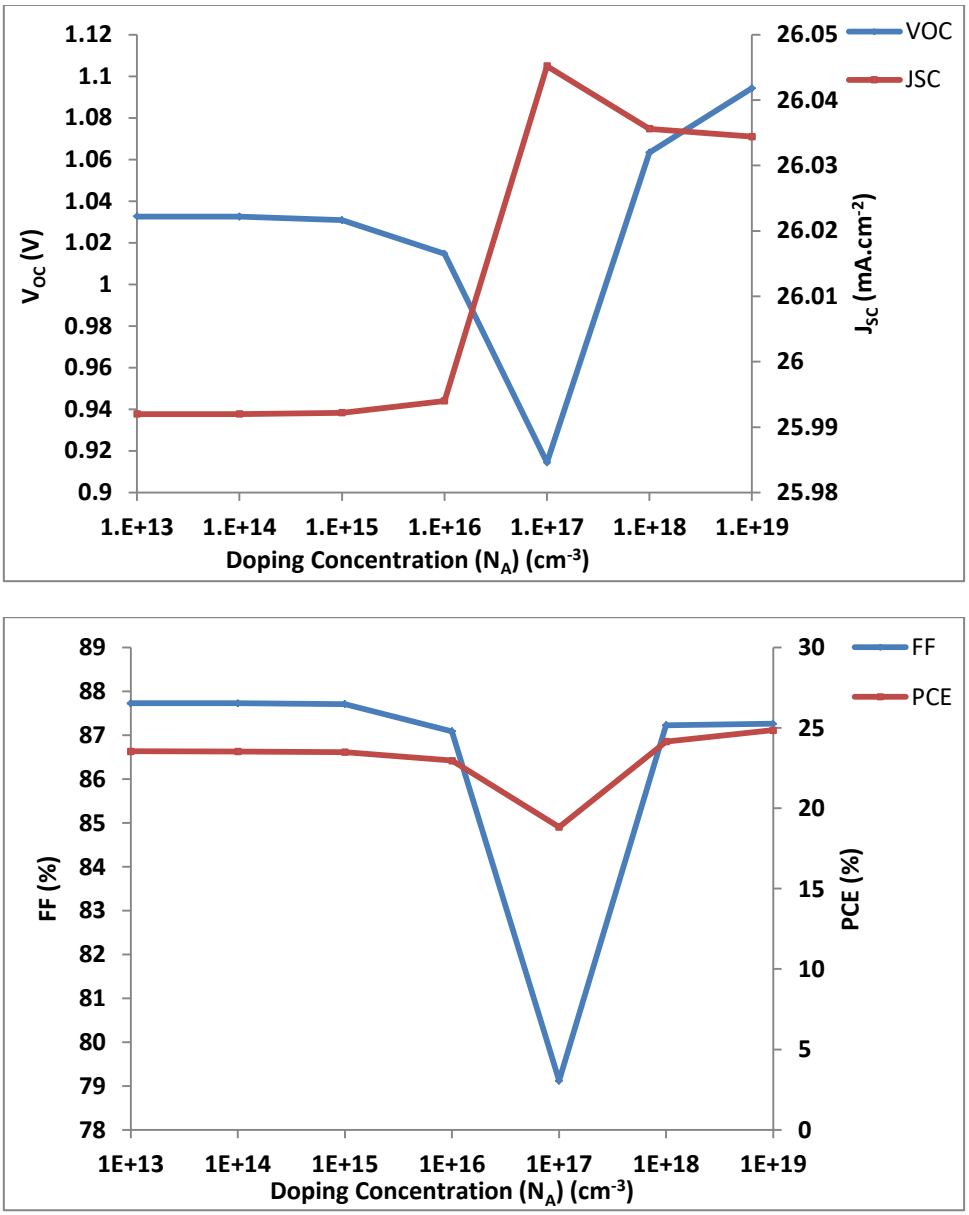

Fig. 6. Variations of V_{oc}, $J_{sc,}$ FF and PCE in terms of the various acceptor concentration (N_A) in HTL materials Cu_2O (colour online)

8. Impact of HTL Defect Density (N_t)

In addition to doping concentration, the defect density (N_t) of the HTL significantly affects the performance of PSCs, as illustrated in Fig. 7. In the range of 10^{11} to 10^{19} cm^{-3}, no notable changes are observed in the characteristic parameters, including V_{OC}, J_{SC} and *PCE*. Higher HTL defect densities, caused by factors like foreign atoms, native defects, and dislocations, introduce shallow or deep traps. These traps act as non-radiative recombination centers, impairing cell performance. Such defects are primarily due to lattice mismatch between the absorber layer and HTL, forming deep traps at the interface that function as Shockley–Read–Hall (SRH) recombination centers. Consequently, PCE drops to about 24.84% at N_t = 10^{19} cm^{-3}. For better performance defect densities to the selection of 10^{17} cm^{-3} for further simulations.

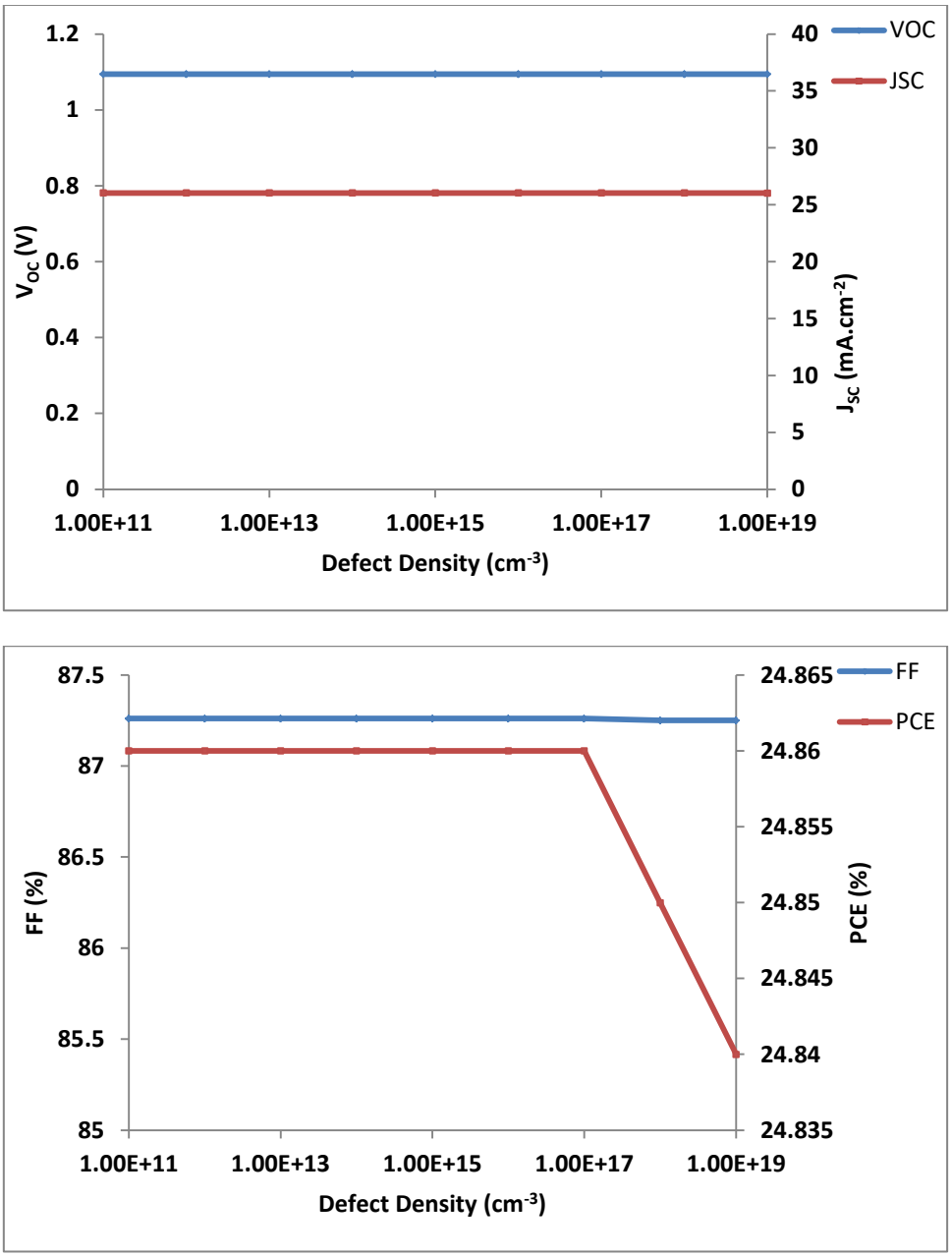

Fig. 7. Effect of defect density of HTL on J_{SC}, V_{OC}, FF, and PCE of perovskite solar cell with Cu_2O (colour online)

9. Impact of ETL thickness

This section examines the effect of ETL thickness on the solar cell's performance by varying it from 25 nm to 400 nm and analysing the corresponding photovoltaic parameters. Fig. 8 presents the results as a function of ETL thickness. The findings indicate that V_{oc}, J_{sc}, *FF* and *PCE* nearly constant and are independent of the ETL thickness up to approximately 225 nm. However, beyond this threshold, the increased thickness requires electrons to travel a longer distance to reach the top electrode, leading to a higher likelihood of electron recombination with minority carriers (holes). Therefore, an ETL thickness of 100 nm is selected for further simulations to balance charge transport and minimize recombination losses.

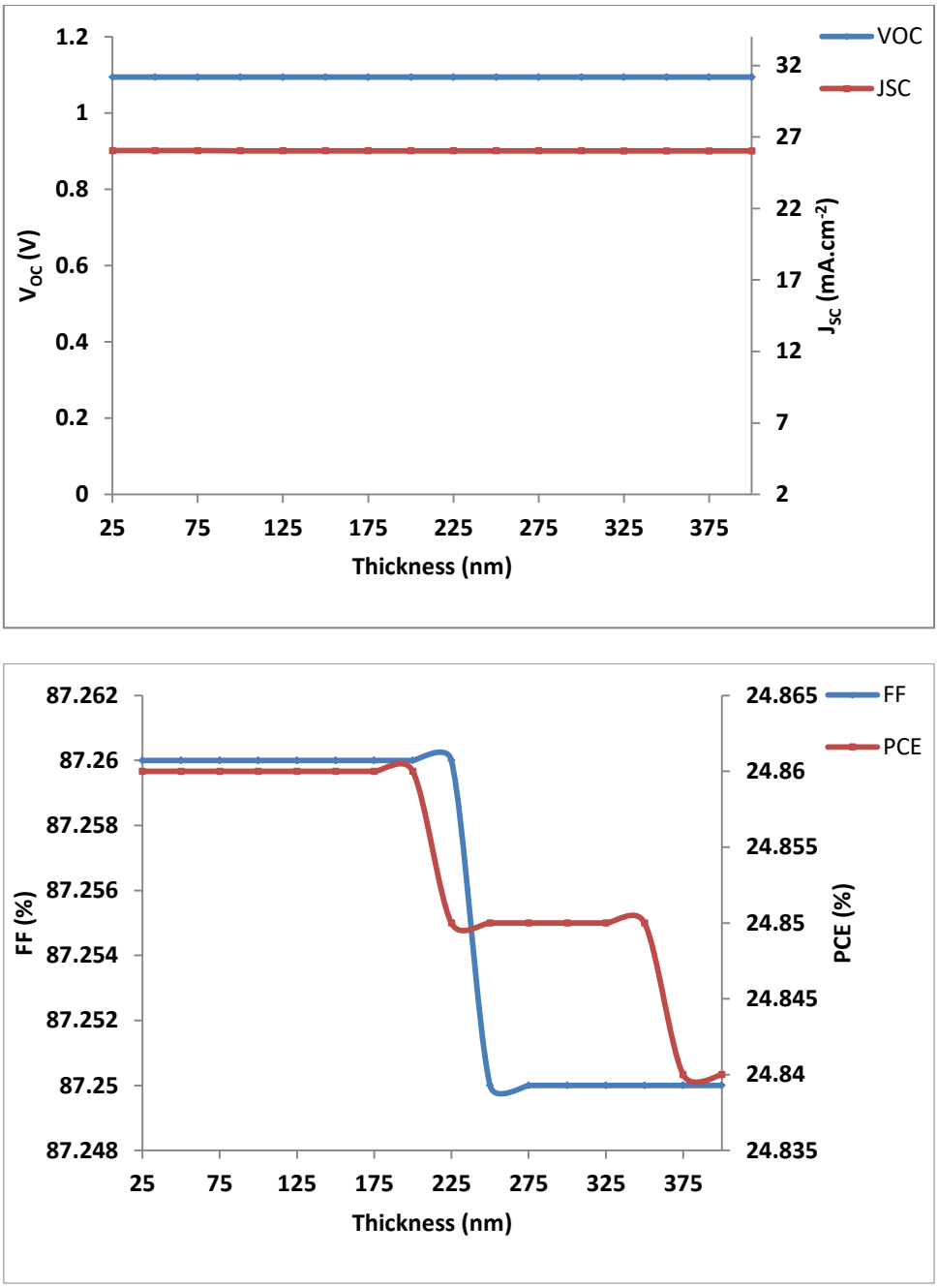

Fig. 8. Variations of V_{oc}, J_{sc}, FF and PCE in terms of the thickness for the ETL materials ZnO (colour online)

10. Impact of ETL Doping Concentration (N_D)

In addition to optimizing the ETL thickness at 100 nm, it is crucial to examine the effect of N_D on the photovoltaic parameters of PSCs. This study investigates the impact of varying N_D from 1×10^{13} cm^{-3} to 1×10^{19} cm^{-3} on the current density–voltage characteristics and *PCE*, as shown in Fig. 9. The results indicate that increasing the doping concentration in the ETL enhances J_{sc} and V_{oc} leading to a higher *PCE*. A peak *PCE* of 24.86% is achieved at a doping concentration of 1×10^{19} cm^{-3}. The improvement in J_{sc} and *FF* is attributed to better energy level alignment between the ETL and the perovskite layer, which enhances charge transport and reduces recombination losses. Although higher doping concentrations improve J_{sc}, *FF*, and overall efficiency, the optimal doping concentration is determined to be 1×10^{19} cm^{-3} due to practical manufacturing challenges. Higher doping levels are difficult to achieve and may introduce deep Coulomb traps, negatively impacting carrier mobility [43].

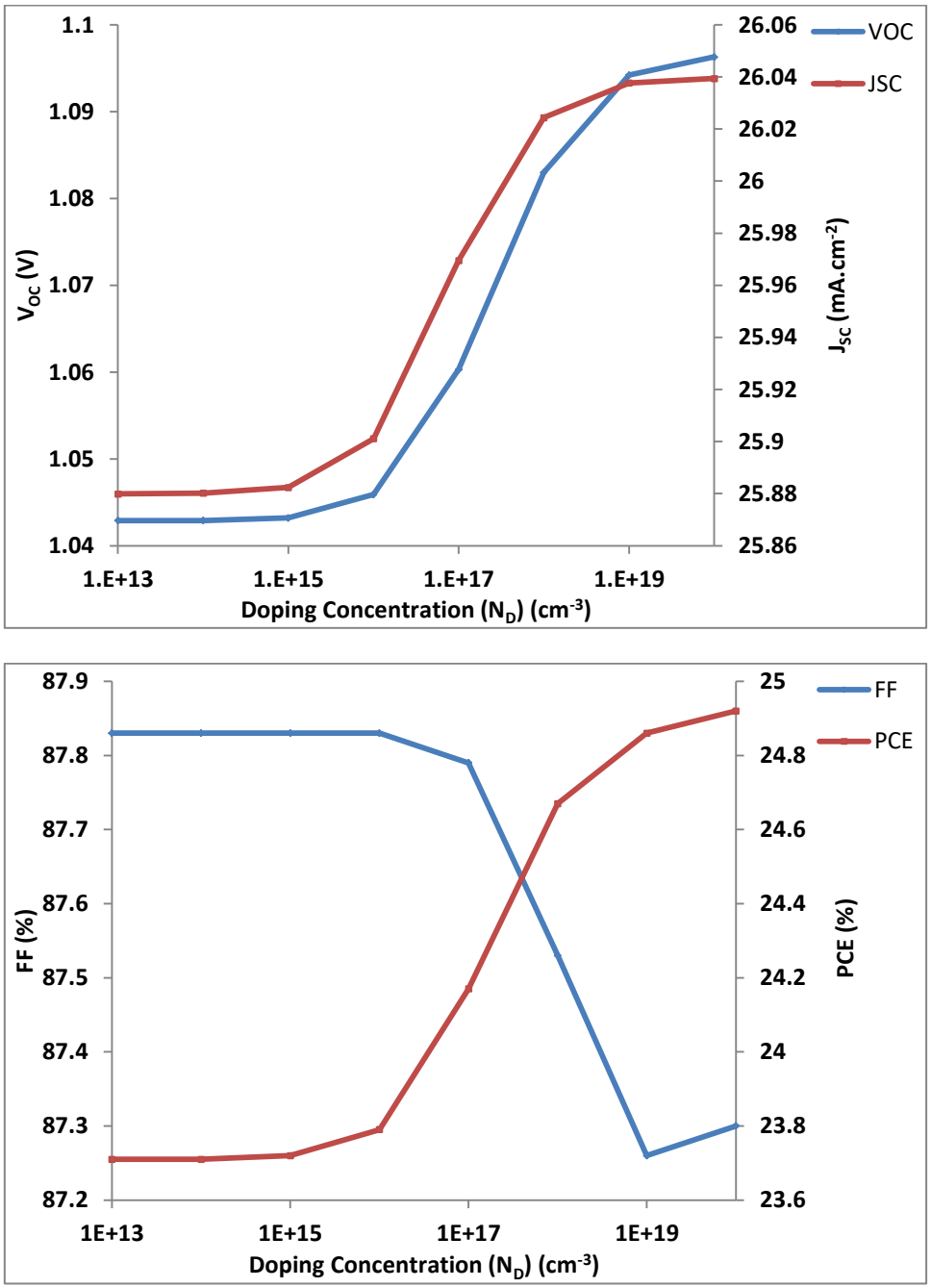

Fig. 9. Variations of V_{oc}, $J_{sc,}$ FF and PCE in terms of the various Doping Concentration (N_D) in ETL materials ZnO (colour online)

11. Impact of ETL defect density

The density of trap states (N_t) in the ZnO layer was varied from 10^{11} to 10^{19} cm^{-3} to evaluate its effect on the power conversion efficiency of the proposed PSC architecture. Fig. 10 shows the influence of N_t variation in the ETL (ZnO) on the key photovoltaic parameters. The results indicate that V_{oc}, J_{sc}, *FF*, and *PCE* remain nearly constant up to an N_t of 10^{15} cm^{-3}. However, beyond this threshold, as N_t increases, J_{sc}, *FF* and *PCE* decrease, reaching values of 25.81 mA/cm², 87.25%, and 24.64%, respectively, at 10^{19} cm^{-3}. The maximum *PCE* achieved is 24.86%. Consequently, an N_t of 10^{13} cm^{-3} is selected for further simulations.

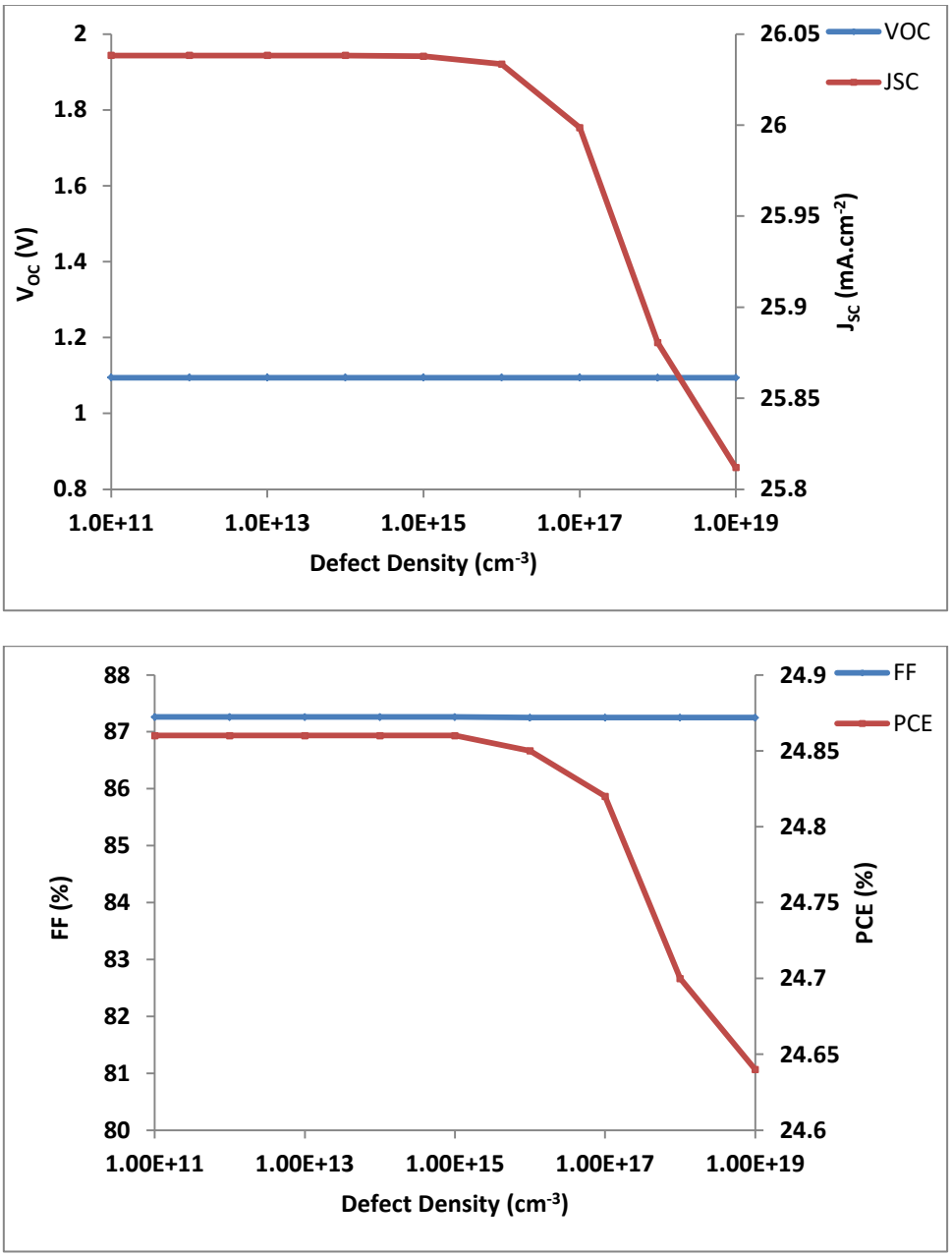

Fig. 10. Influence of defect density (N_t) in ZnO layer on the performance parameters of the proposed solar cell (colour online)

12. Impact of temperature

The performance of the perovskite light absorption layer depends on its electronic structure and microscopic properties, especially the band gap, which influences its light absorption capacity [44-45]. Temperature significantly affects the band gap, with experimental results showing that it increases as temperature rises, impacting the material's photoelectric properties. This change is due to lattice thermal expansion and lattice thermal vibration, leading to higher electron–hole recombination rates and reduced efficiency.

The following equations elucidate the temperature's influence on voltage [46]:

$$V_{oc} = \frac{kT}{q}\left(lnJ_{sc} - \ln\left[BT^3 \exp\left(-\frac{V_g(T)}{V_t}\right)\right]\right)$$

In the given equation, B is a constant independent of time. Two parameters are explicitly defined: the thermal voltage denoted as $V_t = kT/q$, where k is the Boltzmann constant, T is the temperature, and q is the elementary charge; and the energy gap voltage denoted as $V_g = E_g/q$, where E_g is the energy gap. To assess the impact of temperature on the open circuit voltage, it is advisable to derive the equation

$$\frac{dV_{oc}}{dT} = -\frac{(V_{go} - V_{oc}) + 3V_T}{T} + V_T\left(\frac{1}{J_{sc}}\frac{d}{dT}J_{sc} + \frac{1}{V_T}\frac{d}{dT}V_g\right)$$

In the given equation, the first term predominates over the second term, rendering its omission justifiable. Consequently, it is evident that an increase in temperature results in a decrease in the open circuit voltage of PSCs.

Outdoor solar panel deployment exposes them to temperatures above 300 K, causing strain, stress, and interfacial defects, which impair layer connectivity. To assess the impact of operating temperature, simulations were performed from 280 to 400 K, keeping other parameters constant. Fig. 11 shows the variation of cell parameters with temperature. The highest efficiency (~25.89%) was recorded at 280 K, but efficiency decreases with rising temperatures due to reduced hole and electron mobilities and carrier concentration. Interestingly, J_{sc} remains constant with temperature changes, but V_{oc} decreases due to increased interfacial defects, higher series resistance, and shorter carrier diffusion length. At 300 K, the solar cell parameters were V_{OC} = 1.09 V, J_{SC} = 26.04 mA/cm², *FF* = 87.26%, and *PCE* = 24.86%, as illustrated in Fig. 11.

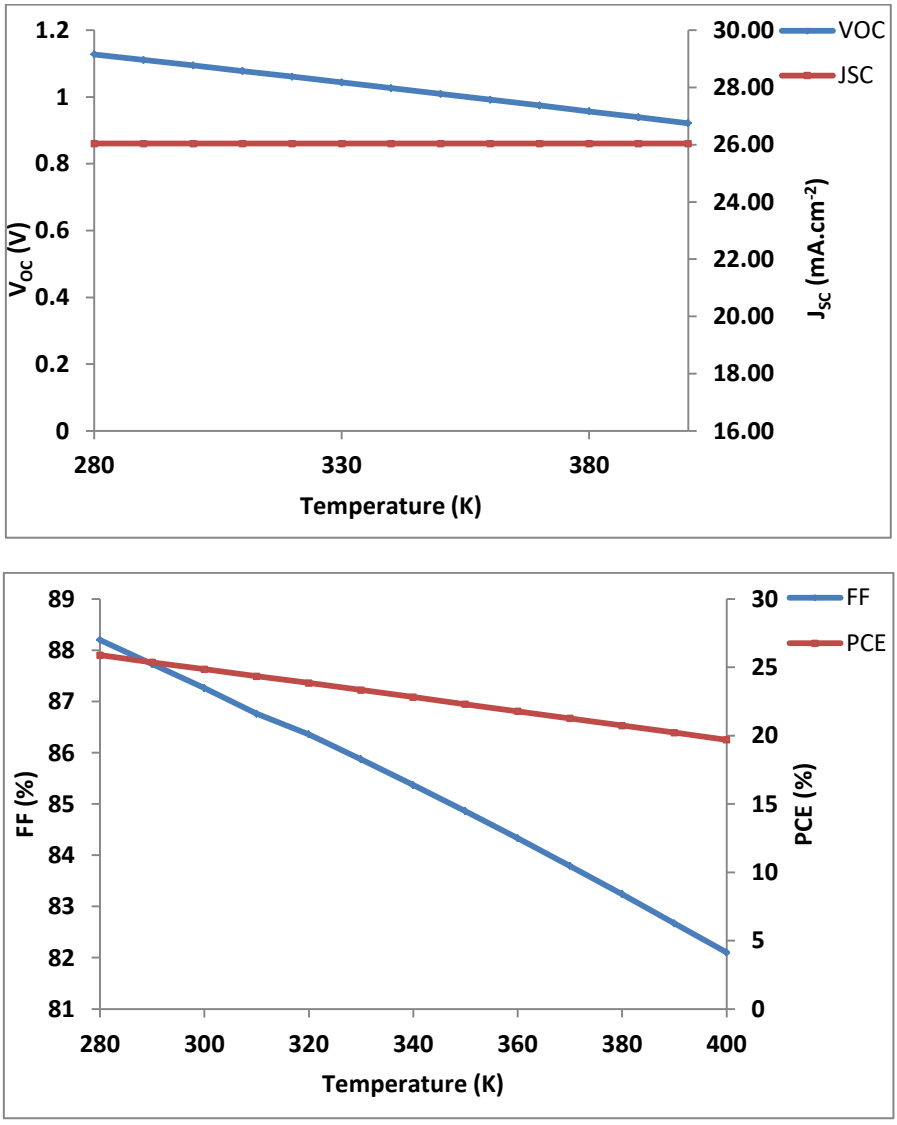

Fig. 11. Effect of the temperature on the V_{OC}, J_{SC}, FF and PCE of the proposed solar cell (colour online)

13. Influence of series and shunt resistances on device performance

Series resistance (R_S) and shunt resistance (R_{SH}) are critical parameters that significantly influence the performance of solar cells. R_S consists of various resistances, including those associated with layer interfaces, metal contacts (both front and back), and the resistance experienced by the current flowing through the emitter and base of the solar cell [47]. Conversely, R_{SH} is primarily due to leakage currents within the device. In Perovskite Solar Cells, R_S arises from internal resistances, interface barriers, charge-collecting interlayers, and metal-based electrodes, whereas R_{SH} is mainly linked to leakage

channels, such as pinholes in the photoactive layer and recombination losses. Figs. 12 and 13 demonstrate the effect of varying R_S (from 0 to 10 Ω·cm²) and R_{SH} (from 1×10^{1} to 1×10^{10} Ω·cm²) on key performance parameters of the solar cell, including Short-Circuit Current Density, Open-Circuit Voltage, Fill Factor, and Power Conversion Efficiency. As R_S increases with a constant R_{SH}, the V_{OC} shows a rising trend, but R_S does not significantly impact J_{SC}. However, FF decreases as R_S increases, consistent with Equation (13) [48]. On the other hand, an increase in R_{SH} leads to a rise in FF due to lower recombination rates [49]. These findings underscore the importance of optimizing R_S and R_{SH} to enhance the efficiency of perovskite solar cells.

$$FF = FF_{ref}\left(1 - R_S\frac{Jsc}{Voc}\right) \tag{6}$$

The reference FF of a solar cell for a given R_S is represented as FF_{ref}. The solar cell conversion efficiency, as shown in Fig. 12, follows a trend similar to that of the fill factor. It is evident from the simulation results that an increase in R_S negatively impacts the efficiency of the solar cell, whereas an increase in shunt resistance significantly enhances efficiency, as illustrated in Fig. 13. These findings highlight the importance of strategic layer arrangement in solar cell design to minimize R_S and maximize R_{SH}. This design approach helps in reducing power losses and enhancing overall device performance. The simulated results indicate that for $RbGeBr_3$ - based solar cells, the values of R_S and R_{SH} are within the ranges of 0 – 10 Ω·cm² and 1×10^{1} to 1×10^{10} Ω·cm², respectively, as depicted in Figs. 12 and 13. This emphasizes the potential of $RbGeBr_3$ as an efficient and reliable material for perovskite solar cells.

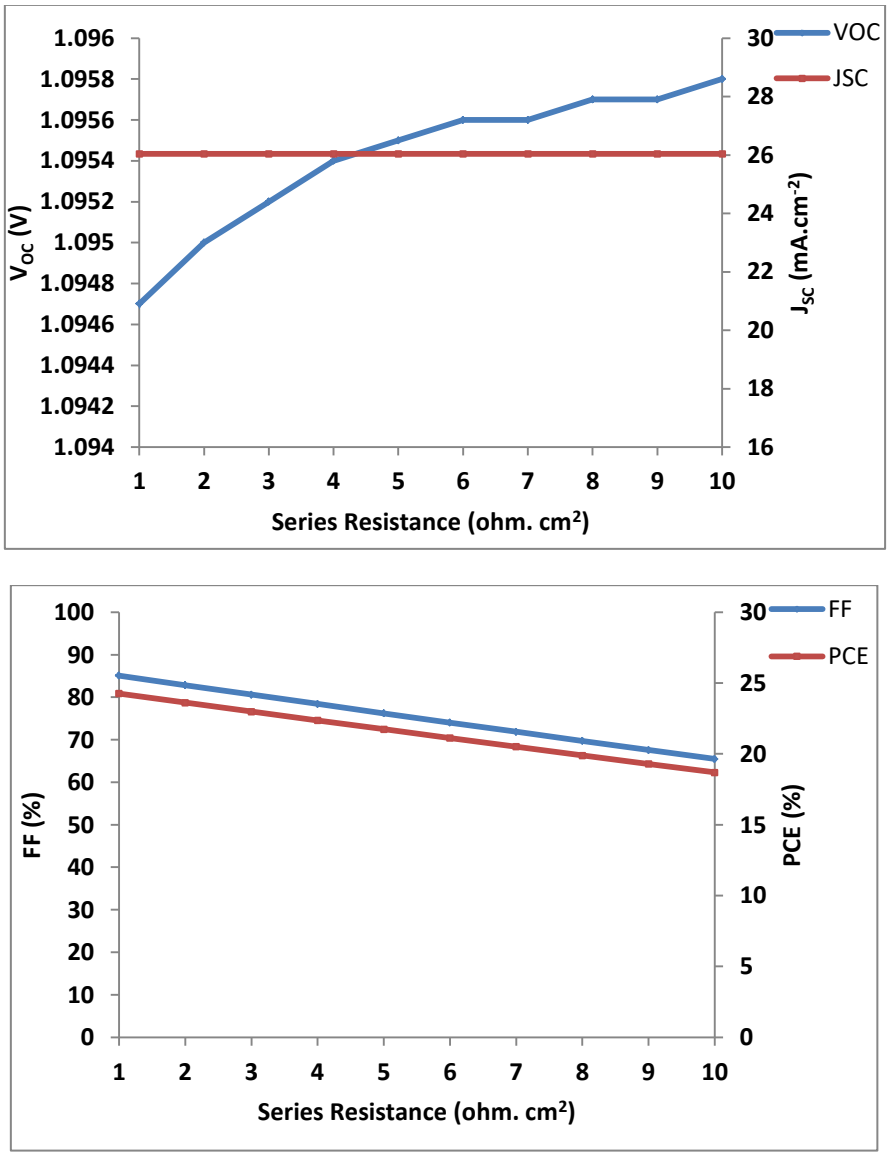

Fig. 12. Effect of series resistance on the solar cell performances of V_{oc}, J_{sc}, FF and PCE (colour online)

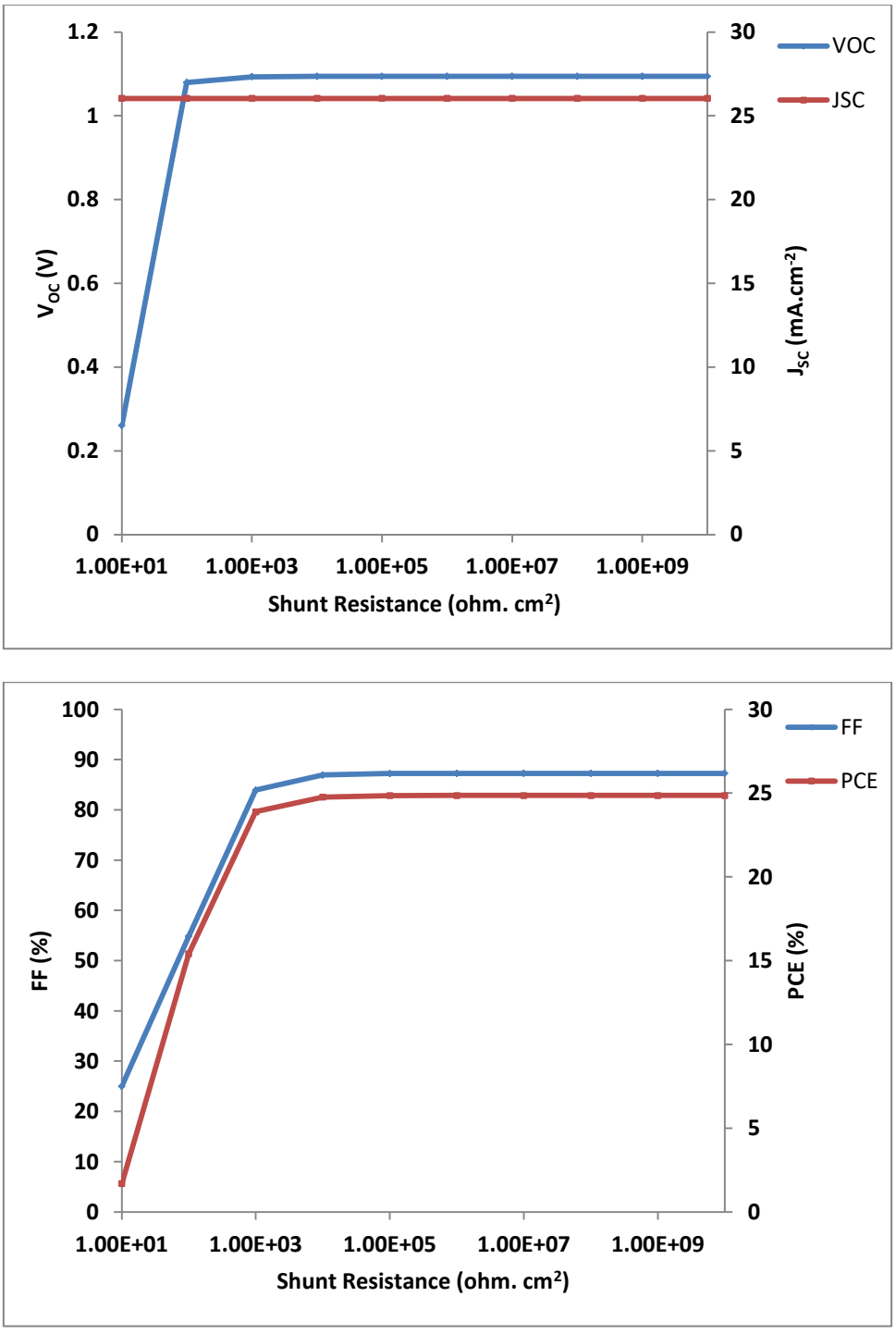

Fig. 13. Effect of shunt resistance on the solar cell performances of V_{oc}, J_{sc}, FF and PCE in (colour online)

14. Quantum efficiency

The Quantum Efficiency (*QE*) response of the proposed solar cell was simulated over a range of photon wavelengths, as shown in Fig. 14. In photovoltaic devices, *QE* represents the ratio of collected charge carriers to the total number of incident photons at a given wavelength on the upper surface of the solar cell. The quantum efficiency to the spectral response *SR(λ)* is given by:

$$QE(\lambda) = SR(\lambda).h.c/(e.\lambda)$$

where *SR(λ)* is the spectral response (A/W), *h* is Planck's constant, *c* is the speed of light, *e* is the elementary charge, *λ* is the wavelength.

This study theoretically investigated the *QE* of the proposed solar cell across a wavelength range of 300 to 900 nm, as illustrated in Fig. 14. The *QE* response can be categorized into two distinct regions for better understanding:

Region I: Spanning from 300 to 360 nm, where the *QE* shows an initial response.

Region II: Extending from 360 to 700 nm, where a high *QE* response of over 90% is observed. This remarkable efficiency is attributed to the exceptional carrier diffusion length of $RbGeBr_3$, approaching the ideal quantum efficiency of 100%.

However, beyond 700 nm, the *QE* declines sharply, as depicted in the figure. This decrease is likely due to the limited absorption of longer wavelengths by the absorber layer, impacting the overall spectral response of the solar cell.

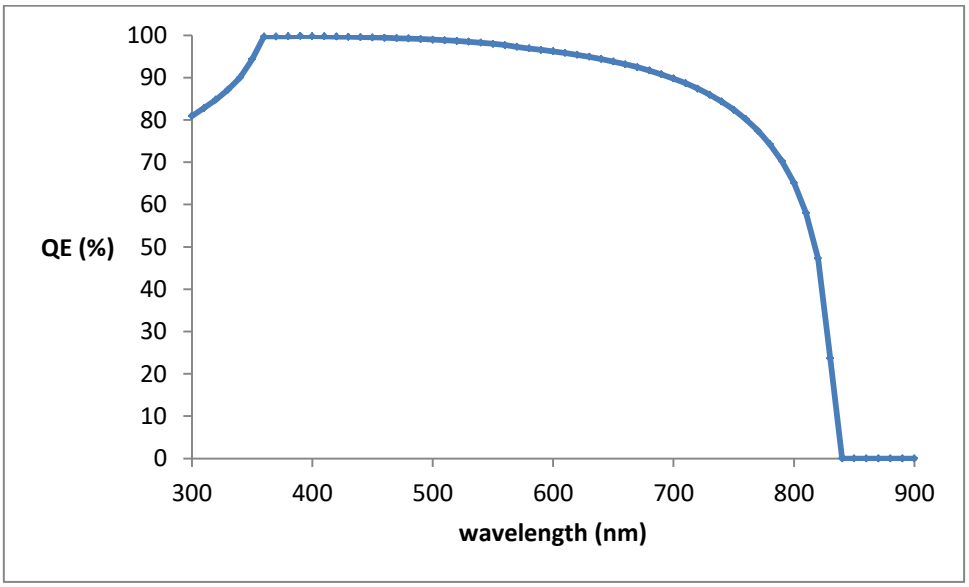

Fig. 14. The response of QE concerning incident photon wavelength for the suggested solar cell (colour online)

15. Optimized result and I–V curve

Efficiency optimization of the ITO/ZnO/$RbGeBr_3$/Cu_2O/Au solar cell structure was achieved by fine-tuning each parameter to its optimal value. Fig. 15 presents the current density – voltage graph of the optimized Perovskite Solar Cell. The initial configuration comprised ITO(100 nm)/ZnO(200 nm)/$RbGeBr_3$(400 nm)/Cu_2O(100 nm)/Au, whereas the optimized configuration featured ITO(100 nm)/ZnO(100 nm)/$RbGeBr_3$(525 nm)/Cu_2O(150 nm)/Au. This optimization led to a significant improvement in Power Conversion Efficiency, with the optimized structure achieving 24.86 compared to 21.17% for the initial design - a remarkable increase of 1.17% times. The enhanced efficiency is attributed to the strategic adjustment of layer thicknesses and material properties, optimizing charge transport and reducing recombination losses. The optimized values for various material parameters, taking into account all optimization aspects, are summarized in Table 3, highlighting the critical adjustments that contributed to the substantial improvement in solar cell performance. Table 4 represents the comparison between this work and others reported work.

Table 3. Optimized Parameters of the proposed solar cell

Physical Parameters	**Symbol**	**Unit**	**Cu_2O (HTL)**	**$RbGeBr_3$ (Absorber Layer)**	**ZnO (ETL)**
Thickness	t	nm	150	525	100
Uniform Shallow Donor Doping	N_D	cm^{-3}	0	1×10^{17}	1×10^{19}
Uniform Shallow Acceptor Doping	N_A	cm^{-3}	1×10^{19}	1×10^{15}	0
Defect Density	N_t	cm^{-3}	1×10^{17}	1×10^{15}	1×10^{13}

Table 4. Comparison between this work and others reported work

Device structure	V_{oc} (V)	J_{sc} (mA/cm^2)	FF (%)	PCE (%)	Ref.
FTO/C60/$RbGeBr_3$/NiO/Au	0.92	22.25	80.20	6.48	[50]
FTO/MoO_3/$KGeCl_3$/WS_2/Au	0.88	41.45	81.76	29.83	[51]
FTO/TiO/RbGeBr/Cu_2O/Ag	1.00	14.476	-	11.92	[52]
FTO/SnS_2/$KGeCl_3$/Cu_2O/C	0.545	41.91	69.24	15.83	[53]
ITO/ZnO/$RbGeBr_3$/Cu_2O/Au	1.09	26.04	87.26	24.86	present work

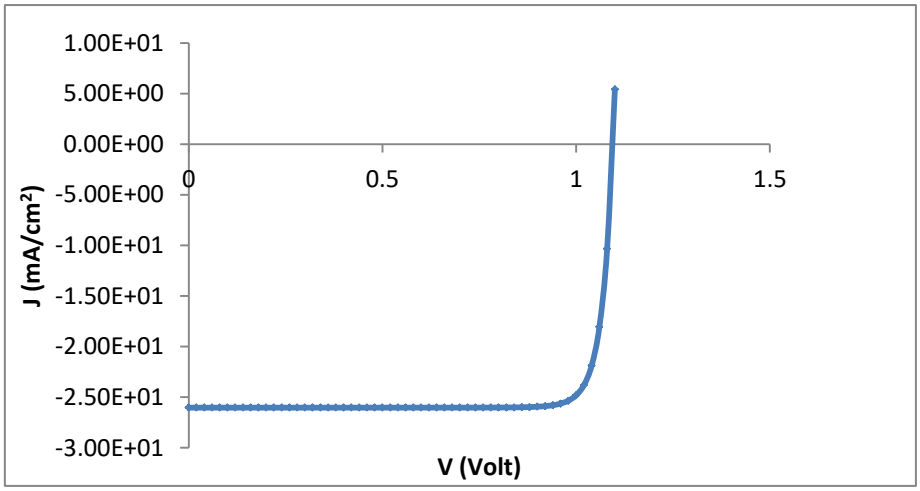

Fig. 15. Current density - voltage curves for the optimized structures (colour online)

16. Energy band alignment

The energy band alignment between the charge transport materials - namely, the Hole Transport Layer and Electron Transport Layer - and the perovskite material is crucial for optimizing the performance of the Perovskite Solar Cell. To enable efficient electron separation from the perovskite, the conduction band of the ETL should align closely with that of the perovskite, ensuring minimal offset, while a significant offset between their valence bands is necessary. If the valence bands are too closely aligned, undesired hole flow to the ETL may occur, increasing the risk of recombination. Similarly, for effective hole separation from the perovskite, the valence band of the HTL should be closely aligned with that of the perovskite, while their conduction bands should have a substantial offset. If the conduction bands are too close, electron flow to the HTL may take place, again leading to recombination. Fig. 16 illustrates the energy band alignment of the PSC, demonstrating how optimal band positioning enhances charge separation and minimizes recombination, thus improving the overall efficiency of the solar cell.

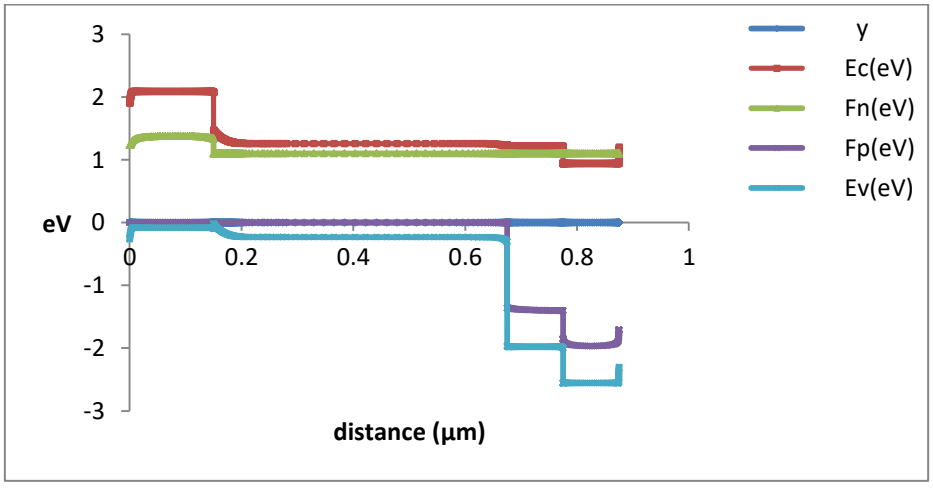

Fig. 16. Energy band alignment of PSC layers (colour online)

17. Conclusions

The proposed solar cell structure, comprising ITO/ZnO/$RbGeBr_3$/Cu_2O/Au, was simulated using the SCAPS-1D program. It was observed that optimizing the thickness, doping concentration, and defect density in all layers could enhance the solar cell's efficiency. The optimized thicknesses for the absorber, HTL, and ETL were found to be 525 nm, 150 nm, and 100 nm, respectively. The donor and acceptor doping concentrations of absorber layer were optimized to 1×10^{17} cm^{-3} and 1×10^{15} cm^{-3} respectively, in case of the ETL the donor doping concentration of 1×10^{19} cm^{-3}, while the HTL utilized an acceptor doping concentration of 1×10^{19} cm^{-3}. These optimizations resulted in a remarkable power conversion efficiency of approximately 24.86%, a short-circuit current density of about 26.04 mA/cm^2, an open-circuit voltage of around 1.09 V, and a fill factor of about 87.26%. These impressive results indicate that the proposed solar cell structure holds significant potential for application in solar cell manufacturing, presenting a viable alternative to conventional lead-based perovskite solar cells. Additionally, the use of $RbGeBr_3$, known for its low cost, non-toxic nature, and material abundance, could contribute to sustainable development by promoting eco-friendly solar energy solutions.

Funding statement

This research did not obtain financial support from any specific grant provided by funding agencies in the public, commercial, or not-for-profit sectors.

Data availability statement

Data will be made available on request.

Declaration of interest's statement

The authors declare no conflict of interest.

Additional information

No additional information is available for this paper.

Acknowledgements

We would like to express our gratitude to Dr. Marc Burgelman and their team from Ghent University, Belgium, for providing access to the SCAPS simulator, which has been instrumental in conducting the simulations for this research.

Institutional Review Board Statement

Not applicable.

Informed Consent Statement: Not applicable.

References

[1] Z. Yang, Y. Guo, H. Li, Y. Zhou, X. Zuo, Y. Yu, C. Pan, J. Strzalka, C.-Y. Nam, M. H. Rafailovich, Adv. Mater. Interfaces **5**, 1800435 (2018).
[2] Nakita K. Noel, Samuel D. Stranks, Antonio Abate, Christian Wehrenfennig, Simone Guarnera, Amir-Abbas Haghighirad, Aditya Sadhanala, Giles E. Eperon, Sandeep K. Pathak, Michael B. Johnston, Annamaria Petrozza, Laura M. Herza, Henry J. Snaith, Energy Environ. Sci. **7**, 3061 (2014).
[3] J. Y. Kim, J.-W. Lee, H. S. Jung, H. Shin, N.-G. Park, Chem. Rev. **120**, 7867 (2020).
[4] Fang-Cheng Liang, Fu-Cheng Jhuang, Yu-Han Fang, Jean-Sebastien Benas, Wei-Cheng Chen, Zhen-Li Yan, Wei-Chun Lin, Chun-Jen Su, Yuki Sato, Takayuki Chiba, Junji Kido, Chi-Ching Kuo, Adv. Mater. **35**, 2207617 (2023).
[5] C. Ma, N.-G. Park, Chem. **6**, 1254 (2020).
[6] A. Abate, Joule **1**, 659 (2017).
[7] R. K. Shukla, A. Srivastava, S. Rani, N. Singh, V. K. Dwivedi, S. Pandey, N. Wadhwani, Integrated Ferroelectrics **240**(1), 73 (2024).
[8] H. Sabbah, J. Arayro, R. Mezher, Materials **15**, 4761 (2022).
[9] K. Xu, Instrum. Sci. Technol. **49**, 91 (2021).
[10] Anchal Srivastava, Navina Wadhwani, R. K. Shukla, Journal of Optics **54**(1), 127 (2025).
[11] W. Ke, M. G. Kanatzidis, Nat. Commun. **10**, 965 (2019).
[12] C. C. Stoumpos, C. D. Malliakas, M. G. Kanatzidis, Inorg. Chem. **52**, 9019 (2013).
[13] K. P. Marshall, M. Walker, R. I. Walton, R. A. Hatton, Nat. Energy **1**, 16178 (2016).
[14] L. M. Herz, ACS Energy Lett. **2**, 1539 (2017).
[15] G. Rajendra Kumar, H.-J. Kim, S. Karupannan, K. Prabakar, J. Phys. Chem. C **121**, 16447 (2017).
[16] Yuqin Liao, Hefei Liu, Wenjia Zhou, Dongwen Yang, Yuequn Shang, Zhifang Shi, Binghan Li, Xianyuan Jiang, Lijun Zhang, Li Na Quan, Rafael Quintero-Bermudez, Brandon R Sutherland, Qixi Mi, Edward H Sargent, Zhijun Ning, J. Am. Chem. Soc. **139**, 6693 (2017).
[17] R. K. Shukla, A. Srivastava, S. Rani, N. Singh, V. K. Dwivedi, S. Pandey, N. Wadhwani, Nanosystems: Physics, Chemistry, Mathematics **15**(1), 135 (2024).
[18] Amrit Kumar Mishra, R. K. Shukla, Materials Today: Proceedings **46**, Part 6, 2288 (2021).
[19] Amrit Kumar Mishra, R. K. Shukla, Materials Today: Proceedings **29**, Part 3, 836 (2020).
[20] A. K. Mishra, R. K. Shukla, SN Appl. Sci. **2**, 321 (2020).
[21] Anyi Mei, Xiong Li, Linfeng Liu, Zhiliang Ku, Tongfa Liu, Yaoguang Rong, Mi Xu, Min Hu, Jiangzhao Chen, Ying Yang, Michael Grätzel, Hongwei Han, Science **345**, 295 (2014).
[22] S. Arya, P. Mahajan, R. Gupta, R. Srivastava, N. K. Tailor, S. Satapathi, R. R. Sumathi, R. Datt, V. A. Gupta, Prog. Solid State Chem. **60**, 100286 (2020).

[23] M. Grätzel, Nat. Mater. **13**, 838 (2014).
[24] P. P. Boix, S. Agarwala, T. M. Koh, N. Mathews, S. G. Mhaisalkar, J. Phys. Chem. Lett. **6**, 898 (2015).
[25] J. E. Jacak, W. A. Jacak, Materials **15**, 2254 (2022).
[26] R. Wu, B. Yang, C. Zhang, Y. Huang, Y. Cui, P. Liu, C. Zhou, Y. Hao, Y. Gao, J. Yang, J. Phys. Chem. C **120**, 6996 (2016).
[27] M. Laska, Z. Krzeminska, K. Kluczyk-Korch, D. Schaadt, E. Popko, W. A. Jacak, J. E. Jacak, Nano Energy **75**, 104751 (2020).
[28] K. Yao, H. Zhong, Z. Liu, M. Xiong, S. Leng, J. Zhang, Y. X. Xu, W. Wang, L. Zhou, H. Huang, A. K. Y. Jen, ACS Nano **13**, 5397 (2019).
[29] S. Shao, J. Liu, G. Portale, H.-H. Fang, G. R. Blake, G. H. ten Brink, L. J. A. Koster, M. A. Loi, Adv. Energy Mater. **8**, 1702019 (2018).
[29] S. J. Lee, S. S. Shin, Y. C. Kim, D. Kim, T. K. Ahn, J. H. Noh, J. Seo, S. I. Seok, J. Am. Chem. Soc. **138**, 3974 (2016).
[30] K. Chen, P. Wu, W. Yang, R. Su, D. Luo, X. Yang, Y. Tu, R. Zhu, Q. Gong, Nano Energy **49**, 411 (2018).
[31] W. Ke, C. C. Stoumpos, M. Zhu, L. Mao, I. Spanopoulos, J. Liu, O. Y. Kontsevoi, M. Chen, D. Sarma, Y. Zhang, M. R. Wasielewski, Sci. Adv. **3**, e1701293 (2017).
[32] F. Wang, J. Ma, F. Xie, L. Li, J. Chen, J. Fan, N. Zhao, Adv. Funct. Mater. **26**, 3417 (2016).
[33] H. Sabbah, J. Arayro, R. Mezher, Nanomaterials **12**, 3885 (2022).
[34] H. Pan, X. Zhao, X. Gong, H. Li, N. H. Ladi, X. L. Zhang, W. Huang, S. Ahmad, L. Ding, Y. Shen, M. Wang, Mater. Horiz. **7**, 2276 (2020).
[35] M. Burgelman, P. Nollet, S. Degrave, Thin Solid Film **361**, 527 (2000).
[36] N. Gamal, S. H. Sedky, A. Shaker, M. Fedawy, Optik **242**, 167306 (2021).
[37] M. S. Rahman, S. Miah, M. S. W. Marma, T. Sabrina, Proceedings of the 2019 International Conference on Electrical, Computer and Communication Engineering (ECCE), Cox's Bazar, Bangladesh, pp. 1–6 (2019).
[38] Karthick Sekar, Latha Marasamy, Sasikumar Mayarambakam, Hesham Hawashin, Mohamad Nourb, Johann Bouclé, RSC Adv. **13**, 25483 (2023).
[39] Shima Valizadeh, Aliasghar Shokri, Amirabbas Sabouri-Dodaran, Nazila Fough, Firdaus Muhammad-Sukki, Results in Physics **57**, 107351 (2024).
[40] Yasin, T. Al Zoubi, M. Moustafa, Optik **229**, 166258 (2021).
[41] S. Aseena, Nelsa Abraham, V. Suresh Babu, Materials Today: Proceedings **43**, Part 6, 3432 (2021).
[42] S. H. Zyoud, A. H. Zyoud, N. M. Ahmed, A. R. Prasad, S. N. Khan, A. F. I. A Bdelkader, M. Shahwan, Crystals **11**, 1468 (2021).
[43] Jinyan Ning, Liangliang Zheng, Wencin Lei, Shenghao Wang, Jinyang Xi, Jiong Yang, Phys. Chem. Chem. Phys. **24**, 16003 (2022).
[44] Pilar Lopez-Varo, Mohamed Amara, Stefania Cacovich, Arthur Julien, Armelle Yaïche, Mohamed Jouhari, Jean Rousset, Philip Schulz, Jean-François Guillemoles, Jean-Baptiste Puel, Sustainable Energy Fuels **5**, 5523 (2021).
[45] G. Siefer, A. W. Bett, Progress in Photovoltaics: Research and Applications **22**, 515 (2014).
[46] N. A. Dumin, K. J. Dickerson, D. J. Dumin, B. T. Moore, Solid State Electron. **39**, 655 (1996).
[47] S. R. A. Ahmed, A. Sunny, S. Rahman, Solar Energy Materials and Solar Cells **221**, article 110919 (2021).
[48] F. F. Muhammad, K. Sulaiman, Thin Solid Films **519**(15), 5230 (2011).
[49] Shima Valizadeh, Aliasghar Shokri, Sani M. Lawal, Nazila Fough, Results in Physics **73**, 108280 (2025).
[50] Ubaid Ur Rehman, Kashaf Ul Sahar, Ejaz Hussain, Chun-Ming Wang, Solar Energy **277**, 112752 (2024).
[51] Ziad Abuwaar, Alaa Elshahat, Hager Zeenelabden, Mohamed Swillam, Samantha Yasin, Marwa Moustafa, Scientific Reports **15**, 1 (2025).
[52] S. Valizadeh, S. M. Lawal, N. Fough, A. A. Shokri, Proceedings of the 31st IEEE (Institute of Electrical and Electronics Engineers) International conference on electronics, circuits, and systems (IEEE ICECS 2024), 18-20 November 2024, Nancy, France. Piscataway: IEEE [online], 10848711. (2024) https://doi.org/10.1109/ICECS61496.2024.10848711.
[53] Md. Adnan Faisal Siddique, Abu Sadat Md. Sayem Rahman, Materials Science and Engineering: B **303**, 117268 (2024).

*Corresponding author: rajeshkumarshukla00@gmail.com